Journal of Materials Chemistry C

ROYAL SOCIETY OF CHEMISTRY

PAPER

View Article Online
View Journal | View Issue

Cite this: J. Mater. Chem. C, 2021, 9, 2047

Manipulation of Cl/Br transmutation in zero-dimensional Mn^{2+}-based metal halides toward tunable photoluminescence and thermal quenching behaviors†

Guojun Zhou, [a] Zhiyang Liu, [b] Maxim S. Molokeev, [cde] Zewen Xiao, [b] Zhiguo Xia [f] and Xian-Ming Zhang *[a]

Received 30th October 2020,
Accepted 26th December 2020

DOI: 10.1039/d0tc05137c

rsc.li/materials-c

Low-dimensional-networked metal halides are attractive for the screening of emitters applied in solid-state lighting and displays, but the lead toxicity and poor stability are obstacles that must be overcome in industrial applications. Herein, we aim at the discovery of bright and stable photoluminescence in zero-dimensional (0D) Mn^{2+}-based metal halides. By manipulation of Cl/Br transmutation, the nature of the halogen can be confirmed as a pivotal factor to tune the PL behaviors, and the optimum Mn^{2+} emission with a high PLQY of 99.8% and a short lifetime of 0.372 ms can be achieved in $(C_{24}H_{20}P)_2MnBr_4$. The thermal quenching behaviors have been discussed in depth, indicating that the synergistic effect of good chemical stability of organic groups, a long Mn···Mn distance of 10.447 Å and a relatively large activation energy (ΔE = 0.277 eV) provides a platform for achieving excellent thermal stability in $(C_{24}H_{20}P)_2MnBr_4$. Moreover, the as-fabricated white LED device with a high luminous efficacy of 118.9 lm W^{-1} and a wide color gamut of 105.3% National Television System Committee (NTSC) shows that $(C_{24}H_{20}P)_2MnBr_4$ can be employed as a desirable narrow-band green emitter for LED displays. This work provides a new understanding of fine tailoring halogens, and proposes a feasible approach to achieving high thermal stability emitters toward the targeted practical applications.

1. Introduction

Organic–inorganic hybrid metal halides (OHMH) have become an emerging hotspot in the field of optical functional materials and devices, but the toxicity of lead and intrinsic instability restrict their further industrial applications.[1–5] Note that the construction and development of high-performance lead-free OHMHs should be emphasized, as well as their abundant photoluminescence (PL) properties, to optimize and meet the requirements of white light-emitting diodes (LEDs) in solid-state lighting and displays.[6–9]

Recently, low-dimensional-networked OHMHs have been the focus of research on bright and stable emitters.[10–13] A variety of organic and inorganic components, the controllable structural dimensions (2D, 1D and 0D), and the doping of luminescent ions can all be used to tune their PL emission, which endows a lot of opportunities and superiorities for the development of white LEDs.[14–17] The possibility of Pb^{2+} being substituted by nontoxic cations (Mn^{2+}, Sn^{2+}, Zn^{2+}, Cu^{2+}, Cu^{+}, Sb^{3+}, *etc.*) can eliminate the barrier of toxicity in the process of industrialization.[8,18–24] However, most low-dimensional-networked OHMHs exhibit PL emission from self-trapped excitons (STEs) with a large Stokes shift,[25] which makes them difficult to excite using

[a] Key Laboratory of Magnetic Molecules and Magnetic Information Materials (Ministry of Education), School of Chemistry and Material Science, Shanxi Normal University, Linfen 041004, China. E-mail: zhangxm@dns.sxnu.edu.cn; Tel: +86-357-2051402
[b] Wuhan National Laboratory for Optoelectronics, Huazhong University of Science and Technology, Wuhan 430074, China
[c] Laboratory of Crystal Physics, Kirensky Institute of Physics, Federal Research Center KSC SB RAS, Krasnoyarsk 660036, Russia
[d] Siberian Federal University, Krasnoyarsk 660041, Russia
[e] Department of Physics, Far Eastern State Transport University, Khabarovsk 680021, Russia
[f] State Key Laboratory of Luminescent Materials and Devices and Institute of Optical Communication Materials, South China University of Technology, Guangzhou 510641, China

† Electronic supplementary information (ESI) available: Details of method and addition figures and tables. PXRD patterns of $(C_{24}H_{20}P)_2MnCl_{4-x}Br_x$ (x = 0, 1, 2, 3, 4) for Fig. S1; photographs of $(C_{24}H_{20}P)_2MnCl_{4-x}Br_x$ (x = 0, 1, 2, 3, 4) single crystals for Fig. S2; local structures of $[MnX_4]^{2-}$ (X = Cl/Br) for Fig. S3; experimental bandgaps and calculated optical absorption spectra of $(C_{24}H_{20}P)_2MnCl_{4-x}Br_x$ (x = 0 and 4) for Fig. S4 and S5; temperature-dependent PL spectra of $(C_{24}H_{20}P)_2MnCl_{4-x}Br_x$ (x = 0, 1, 2, 3, 4) for Fig. S6. TG curves of $(C_{24}H_{20}P)_2MnCl_{4-x}Br_x$ (x = 0, 1, 2, 3, 4) for Fig. S7; time-dependent PL spectra of $(C_{24}H_{20}P)_2MnBr_4$ in an 85% humidity environment for Fig. S8; time-dependent emission intensity of the fabricated LED based on $(C_{24}H_{20}P)_2MnBr_4$ and blue chip for Fig. S9. Crystallographic data of $(C_{24}H_{20}P)_2MnCl_{4-x}Br_x$ (x = 0, 1, 2, 3, 4) (CIF). CCDC 2048395–2048399. For ESI and crystallographic data in CIF or other electronic format see DOI: 10.1039/d0tc05137c

blue light, thereby limiting the luminous efficiency of white LED devices. Meanwhile, the poor thermal stability is another intuitively negative factor restricting their application in the LED area. Finding bright and stable emitters remains a tricky and immense challenge. Remarkably, an emerging alternative is zero-dimensional (0D) Mn^{2+}-based OHMHs with a near-unity photoluminescence quantum yield (PLQY).[26–34] Divalent manganese (Mn^{2+}) is an important luminescent ion, whose emission color is dependent on its coordination environment. Six-coordinated Mn^{2+} exhibits broad-band orange-red emission, whereas four-coordinated Mn^{2+} shows narrow-band green emission.[35] In particular, narrow-band green emitters present huge demand in solid-state displays. Kovalenko *et al.* reported a series of Mn^{2+}-based/doped fully inorganic and hybrid metal halides, which all exhibit bright green emission with a full width at half maximum (fwhm) of 40–60 nm and relatively high PLQYs of 70–90%.[27] Seshadri *et al.* and Xia *et al.* further found a correlation between the Mn···Mn distances and PLQYs to unravel the near-unity green emission in 0D Mn^{2+}-based OHMHs, where the high PLQY is associated with a long Mn···Mn distance.[28,29] However, the effect of finely tailoring the halogens (Cl and Br) on the PL behaviors has not been discussed. More to the point, there is no in-depth evaluation and analysis of the thermal stability of such materials, which is a crucial research subject to guide their practical application in solid-state lighting and displays.

In this work, we first emphasize the effect of finely tailoring the halogens (Cl and Br) on the PL behaviors of the emission wavelengths, lifetimes, and PLQYs, taking $(C_{24}H_{20}P)_2MnCl_{4-x}Br_x$ (x = 0, 1, 2, 3, 4) as a case. Consequently, the nature of the halogen is confirmed as a core factor to tune the PL, and the optimum Mn^{2+} emission with a high PLQY of 99.8% and a short lifetime of 0.372 ms can be achieved in $(C_{24}H_{20}P)_2MnBr_4$. Importantly, we further evaluate the electronic features and optical absorption according to density functional theory (DFT) calculations, and elaborate the thermal quenching behaviors from the perspectives of chemical stability and crystal structure. Not only that, a white LED device with a high luminous efficacy of 118.9 lm W^{-1} and a wide color gamut of 105.3% National Television System Committee (NTSC) can be fabricated based on a green emitter of $(C_{24}H_{20}P)_2MnBr_4$, a red emitter of K_2SiF_6:Mn^{4+} and an InGaN blue chip (λ_{max} = 450 nm). Our realizable cases expose a new understanding of fine tailoring of halogens and thermal quenching behaviors toward the discovery of high-performance low-dimensional lead-free emitters in solid-state lighting and displays.

2. Experimental section

2.1 Materials and preparation

All purchased materials and solvents are as follows: tetraphenylphosphonium chloride ($C_{24}H_{20}PCl$, 98%, Aladdin), tetraphenylphosphonium bromide ($C_{24}H_{20}PBr$, 98%, Aladdin), manganese chloride ($MnCl_2$, 99%, Aladdin), manganese chloride tetrahydrate ($MnBr_2 \cdot 4H_2O$, 98%, Aladdin), *N*,*N*-dimethylformamide (DMF, 99.5%, Aladdin), and ethyl ether ($C_4H_{10}O$, 99.7%, Sinopharm). $MnBr_2 \cdot 4H_2O$ needs to be heated at 120 °C for 6 h to remove the crystal water for later use. $(C_{24}H_{20}P)_2MnCl_{4-x}Br_x$ (x = 0, 1, 2, 3, 4) were synthesized by dissolving a desired amount of $C_{24}H_{20}PCl$/$C_{24}H_{20}PBr$ and $MnCl_2$/$MnBr_2$ into 2 mL DMF under vigorous stirring at 50 °C. The heating was stopped, and ethyl ether was added to the above DMF solution, and it was filtered to form the powder products, which were then dried at 60 °C for 24 h. If ethyl ether slowly diffused into the DMF solution at room temperature (RT), the single-crystal products were gradually precipitated. Finally, $(C_{24}H_{20}P)_2MnBr_4$, K_2SiF_6:Mn^{4+} and an InGaN blue chip were used to fabricate LED devices.

2.2 Characterization

Powder X-ray diffraction (PXRD) patterns were collected using an Aeris powder diffractometer (PANalytical Corporation) with Cu-Kα radiation (λ = 1.5406 Å), operating at 40 kV and 15 mA. The step size of 2θ was 0.011°, and the counting time was 2 s per step. Rietveld refinements were performed using TOPAS 4.2. Single-crystal X-ray diffraction data were collected on an Agilent Technologies Gemini EOS diffractometer at RT using Mo-Kα radiation (λ = 0.71073 Å). Photoluminescence excitation/emission (PLE/PL) spectra, PL decay curves, and photoluminescence quantum yields (PLQYs) were obtained by using an FLSP9200 fluorescence spectrophotometer at RT. Temperature-dependent spectra were measured on a Hitachi F-4600 fluorescence spectrophotometer with a heating apparatus as the heating source. Diffuse reflectance spectra were measured on a Hitachi UH4150 UV-vis-near-infrared spectrophotometer, and $BaSO_4$ was used for calibration. Thermogravimetric analysis (TGA) was performed on SETARAM 131 LABSYS equipment under an argon stream with a heating rate of 10 °C min^{-1} from RT to 800 °C. The emission spectra, correlated color temperature (CCT), luminous efficacy, and CIE coordinates of the LED devices were measured on an integrating sphere spectroradiometer system (ATA-100, Everfine).

2.3 Computational methods

Density functional theory (DFT) calculations were performed by using the Vienna Ab initio Simulation Package (VASP)[36–38] and projector-augmented-wave (PAW)[39,40] potential. The original structures were obtained by experiments, and they were optimized using the semilocal Perdew–Burke–Ernzerhof (PBE) functional within the generalized-gradient approximation (GGA).[41] Γ-Centered 2 × 1 × 1 k-meshes were used to sample the Brillouin zone. To correct the van der Waals interactions, the DFT-D3 correction method of Grimme[42,43] was employed. The kinetic energy cut-off for the electron wave functions was 400 eV and all structures were fully relaxed until the force on each atom was <0.03 eV $Å^{-1}$. For electronic calculations, a more advanced Heyd–Scuseria–Ernzerhof (HSE)[44] hybrid functional was used to exchange and correlate, which provided accurate results in electronic properties in our former hybrid organic–inorganic halide perovskites.[29]

3. Results and discussion

3.1 Synthesis and structure evolution

Metal halides of $(C_{24}H_{20}P)_2MnCl_{4-x}Br_x$ (x = 0, 1, 2, 3, 4) are synthesized by the co-precipitation method, and the ratio of the Cl and Br contents can be manipulated specifically by designing different raw materials. Fig. 1a depicts the crystal structure of $(C_{24}H_{20}P)_2MnCl_{4-x}Br_x$ (x = 0, 1, 2, 3, 4), where the isolated tetrahedron of $[MnX_4]^{2-}$ is surrounded by $C_{24}H_{20}P$ organic molecules. This unique structure makes it possible for 0D Mn^{2+}-based halides to have a long Mn···Mn distance, leading to highly-efficient narrow-band green emission from tetrahedrally coordinated Mn^{2+}, which highlights good application prospects in LED displays. As shown in Fig. S1 (ESI†), the PXRD patterns of $(C_{24}H_{20}P)_2MnCl_{4-x}Br_x$ (x = 0, 1, 2, 3, 4) were collected at RT, and the characteristic diffraction peaks gradually shifting to lower angles indicate qualitatively that the cell volume is increasing with the replacement of Cl by Br. All peaks can be indexed to a monoclinic cell ($C2/c$) with parameters close to previously known $(C_{24}H_{20}P)_2MnBr_4$.[26] Meanwhile, we also synthesized single-crystals of $(C_{24}H_{20}P)_2MnCl_{4-x}Br_x$ (x = 0, 1, 2, 3, 4) (Fig. S2, ESI†), and the crystallographic information files (CIFs) are presented in the ESI.† In addition, the powder refinements performed using TOPAS 4.2 (Table 1 and Fig. 1b–g) show an isomorphic structure and linearly increasing cell volume with x(Br) increasing. This is in good agreement with the fact that the Br ion is bigger than the Cl ion and proves that the suggested chemical formula is close to the real one. Therefore, fine tailoring of halogens can be realized in this 0D Mn^{2+}-based metal halide, which provides an experimental basis for designing bright and stable narrow-band green emission by Cl/Br transmutation.

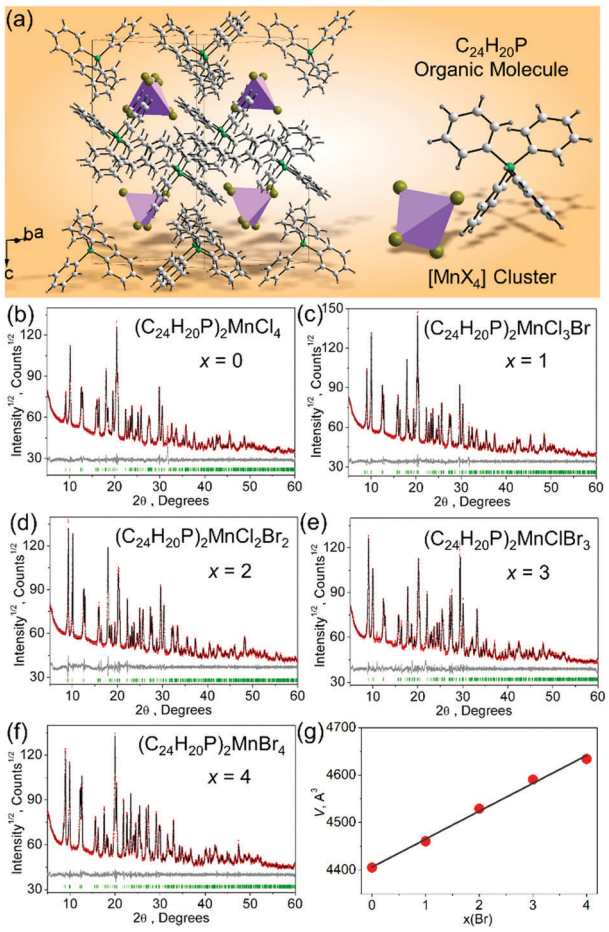

Fig. 1 (a) The crystal structure of $(C_{24}H_{20}P)_2MnCl_{4-x}Br_x$ in which the $[MnX_4]^{2-}$ isolated tetrahedron is surrounded by $C_{24}H_{20}P$ organic molecules. Difference Rietveld plot of $(C_{24}H_{20}P)_2MnCl_{4-x}Br_x$: (b) x = 0; (c) x = 1; (d) x = 2; (e) x = 3; and (f) x = 4. (g) Linear cell volume increasing with increasing x(Br) concentration.

3.2 Tunable photoluminescence and electronic structure

In what follows, the optical properties of $(C_{24}H_{20}P)_2MnCl_{4-x}Br_x$ (x = 0, 1, 2, 3, 4) affected by manipulation of Cl/Br transmutation are discussed. From the normalized photoluminescence excitation (PLE) and photoluminescence (PL) spectra in Fig. 2a, a series of Mn^{2+}-based halides $(C_{24}H_{20}P)_2MnCl_{4-x}Br_x$ (x = 0, 1, 2, 3, 4) all exhibit green emission peaks of 515 nm under excitation at 365 nm. The PLE spectra monitored at 515 nm show three distinct bands from 200 to 500 nm, which correspond to the unique electronic transitions of tetrahedrally coordinated Mn^{2+} ions.[45] Accordingly, $(C_{24}H_{20}P)_2MnCl_{4-x}Br_x$ (x = 0, 1, 2, 3, 4) show narrow-band emission with a fwhm of 46 nm, which is derived from the d–d transition ($^4T_1 \rightarrow {}^6A_1$) of tetrahedrally coordinated Mn^{2+} ions. As shown in Fig. S3 (ESI†), the Mn^{2+} ions are always four-coordinated with halogen ions of Cl/Br, which forms a relatively stable crystal field environment for Mn^{2+} centers, and thus the emission wavelengths of $(C_{24}H_{20}P)_2MnCl_{4-x}Br_x$ (x = 0, 1, 2, 3, 4) remain unchanged with the replacement of Cl by Br. Compared with the commercial narrow-band green-emitting β-Sialon:Eu^{2+},[46] the PL spectra of $(C_{24}H_{20}P)_2MnCl_{4-x}Br_x$ (x = 0, 1, 2, 3, 4) are narrower, which enables them to achieve a wide color gamut for liquid crystal displays (LCDs) in solid-state displays.[47] Fig. 2b presents the decay curves under excitation at 365 nm, monitored at 515 nm. Among them, the decay curves of $(C_{24}H_{20}P)_2MnCl_4$ and $(C_{24}H_{20}P)_2MnBr_4$ are fitted by a single-exponential function: $I(t) = I_0 + A\exp(-t/\tau)$. On the contrary, the decay curves of $(C_{24}H_{20}P)_2MnCl_{4-x}Br_x$ (x = 1, 2, 3) are fitted by a double-exponential function: $I = A_1\exp(-t/\tau_1) + A_2\exp(-t/\tau_2)$, and the average lifetimes can be obtained by using the calculation formula $\tau = (A_1\tau_1^2 + A_2\tau_2^2)/(A_1\tau_1 + A_2\tau_2)$. We speculate that the hybridization of Cl and Br leads to an additional non-radiative transition channel, such as vacancy defects, thereby reducing their luminous efficiency. In consideration of previous work,[48] the formation energy of Cl vacancies is lower than that of Br vacancies, further indicating that the increase of Br inhibits the formation of defects, which in turn contributes to the improvement of the PLQYs. In fact, as shown in Fig. 2c, the PLQYs of $(C_{24}H_{20}P)_2MnCl_{4-x}Br_x$ (x = 0, 1, 2, 3, 4) under 450 nm excitation show an increasing trend with the replacement of Cl by Br, and $(C_{24}H_{20}P)_2MnBr_4$ exhibits the highest PLQY of 99.8%. Moreover, the variation of the green emission intensity can be given intuitively under 365 nm lamp irradiation (Fig. 2d), which verifies the brightest green luminescence of Mn^{2+} in $(C_{24}H_{20}P)_2MnBr_4$.

Table 1 Main parameters of the processing and refinement of $(C_{24}H_{20}P)_2MnCl_{4-x}Br_x$ (x = 0, 1, 2, 3, 4) powders

x	Space group	Cell parameters (Å), volume (Å^3)	R_{wp}, R_p, R_B, χ^2
0	$C2/c$	a = 11.0782 (17), b = 19.529 (3), c = 20.370 (3), V = 4405.1 (11)	3.57, 2.49, 0.12, 1.86
1	$C2/c$	a = 11.1307 (8), b = 19.5916 (18), c = 20.4642 (12), V = 4460.7 (6)	3.00, 2.30, 0.1, 1.70
2	$C2/c$	a = 11.2004 (13), b = 19.671 (3), c = 20.562 (2), V = 4528.1 (1)	3.65, 2.75, 0.15, 2.10
3	$C2/c$	a = 11.2683 (13), b = 19.725 (3), c = 20.666 (3), V = 4590.3 (11)	3.25, 2.39, 0.11, 1.96
4	$C2/c$	a = 11.3266 (7), b = 19.7842 (14), c = 20.6981 (14), V = 4634.3 (5)	2.58, 2.01, 0.07, 1.59

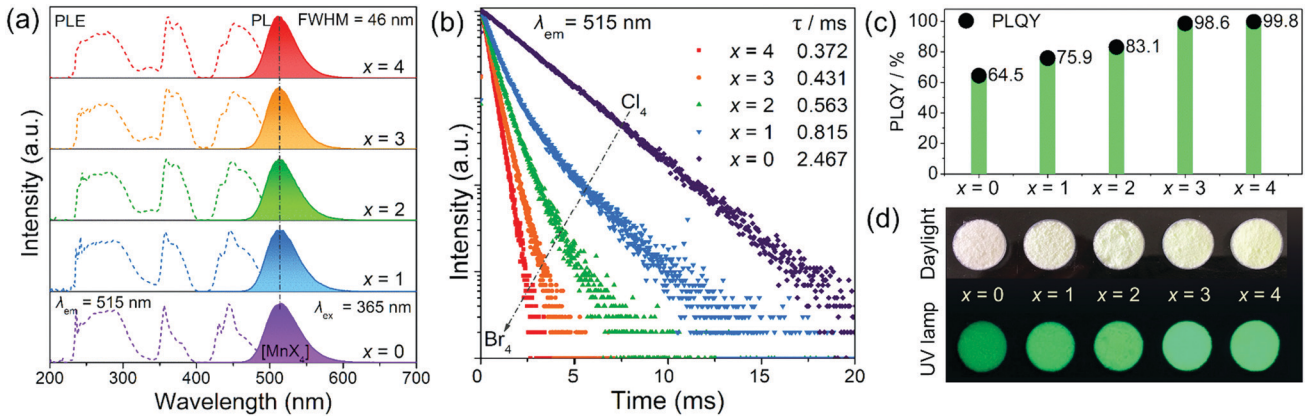

Fig. 2 (a) Normalized photoluminescence (PL) and photoluminescence excitation (PLE) spectra of $(C_{24}H_{20}P)_2MnCl_{4-x}Br_x$ (x = 0, 1, 2, 3, 4). (b) PL decay curves of $(C_{24}H_{20}P)_2MnCl_{4-x}Br_x$ (x = 0, 1, 2, 3, 4) under excitation at 365 nm, monitored at 640 nm, and their lifetimes, which gradually decrease with the replacement of Cl atoms by Br. (c) PLQY dependence on the halogen contents (Cl and Br) for $(C_{24}H_{20}P)_2MnCl_{4-x}Br_x$ (x = 0, 1, 2, 3, 4) under 450 nm excitation, and $(C_{24}H_{20}P)_2MnBr_4$ exhibiting the highest PLQY of 99.8%. (d) Photographs of $(C_{24}H_{20}P)_2MnCl_{4-x}Br_x$ (x = 0, 1, 2, 3, 4) under daylight and a UV lamp of 365 nm.

Narrow-band emitters with relatively short fluorescence lifetimes can weaken the image-retention phenomenon so that they can be well used in fast-response backlight displays.[49] As shown in the inset of Fig. 2b, the values of the lifetimes are calculated to be 2.467, 0.815, 0.563, 0.431, and 0.372 ms, corresponding to x = 0, 1, 2, 3, and 4, respectively. This not only proves that the narrow-band green emission is derived from the $^4T_1$–$^6A_1$ transition of Mn^{2+}, but also confirms that the lifetimes of Mn^{2+} decrease gradually with the replacement of Cl by Br. Accordingly, high-performance narrow-band green emission with a short lifetime of 0.372 ms can be achieved in $(C_{24}H_{20}P)_2MnBr_4$, which shows great application prospects in solid-state displays.

The electronic features of the $(C_{24}H_{20}P)_2MnCl_{4-x}Br_x$ (x = 0, 4) compounds were calculated using the HSE functional, as shown in Fig. 3. The calculated bandgap of $(C_{24}H_{20}P)_2MnCl_4$ is 3.64 eV, slightly larger than that of $(C_{24}H_{20}P)_2MnBr_4$ (3.57 eV). This is in line with experimental trends, *i.e.* 4.13 and 3.82 eV, respectively (Fig. S4, ESI†). We could also find that among these compounds, the valence band maximum (VBM) mainly consists of halogen p and Mn d orbitals, while the conduction band minimum (CBM) is mainly contributed by the organic molecule $(C_{24}H_{20}P)$ p orbitals. Besides, the sharp peaks near the VBM indicate that the valence bands of $(C_{24}H_{20}P)_2MnCl_4$ and $(C_{24}H_{20}P)_2MnBr_4$ are nearly dispersionless, showing negligible electronic coupling between $[MnX_4]^{2-}$ clusters.[50] In addition, the optical absorption properties of these compounds were also investigated by the HSE method. We calculated the absorption coefficient using the following formula: $\alpha = \omega\sqrt{2\left(\sqrt{\varepsilon_1^2+\varepsilon_2^2}-\varepsilon_1\right)}$, where ε_1 and ε_2 are the real and imaginary parts of the complex dielectric function,

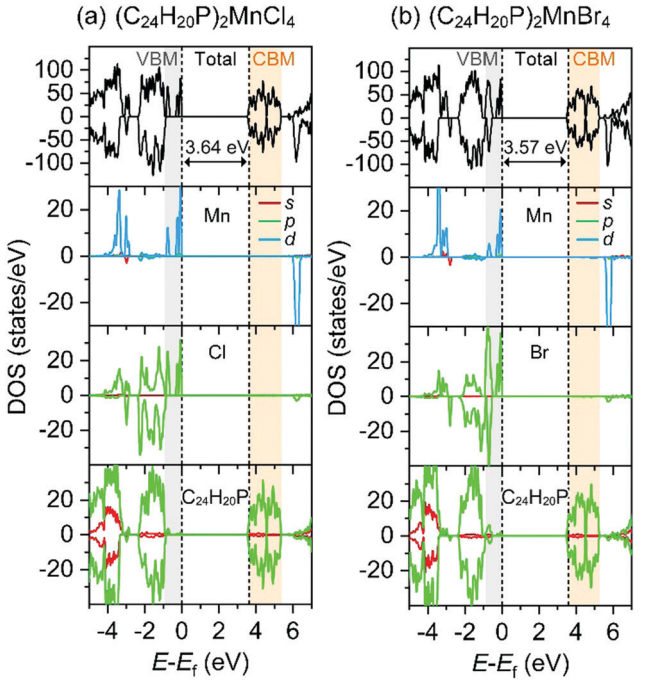

Fig. 3 HSE calculated total and projected densities of states of (a) $(C_{24}H_{20}P)_2MnCl_4$ and (b) $(C_{24}H_{20}P)_2MnBr_4$.

respectively. As depicted in Fig. S5 (ESI†), the absorption of both $(C_{24}H_{20}P)_2MnCl_4$ and $(C_{24}H_{20}P)_2MnBr_4$ starts at about 4 eV, which is in the ultraviolet range.

3.3 Thermal quenching property and application for LEDs

Thermal stability is another critical criterion for evaluating the performance of luminescent materials in LED applications. Temperature-dependent PL spectra of $(C_{24}H_{20}P)_2MnCl_{4-x}Br_x$ (x = 0, 1, 2, 3, 4) under 365 nm excitation are shown in Fig. S6a–e (ESI†). Unsurprisingly, the emission intensity of Mn^{2+} decreases with the increase of the temperature from RT to 200 °C, and the thermal stability is gradually optimized with the replacement of Cl by Br (Fig. S6f, ESI†). The thermogravimetric (TG) results in Fig. S7 (ESI†) further show that their chemical stability is improved with the increase of Br.

As the most excellent narrow-band green emitter, $(C_{24}H_{20}P)_2MnBr_4$ not only shows a high PLQY of 99.8% and a short lifetime of 0.372 ms, but also shows the best thermal stability. Accordingly, the corresponding thermal quenching property of $(C_{24}H_{20}P)_2MnBr_4$ is discussed in detail. As illustrated in Fig. 4a, the emission intensity of $(C_{24}H_{20}P)_2MnBr_4$ at 200 °C still retains 82.6% of that at RT, showing unprecedented excellent thermal stability compared with almost all metal halides previously reported.[51–53] To fully explain the thermal quenching mechanism, the TG curve in Fig. 5a first indicates that $(C_{24}H_{20}P)_2MnBr_4$ is stable before 425 °C. When the temperature continues to rise above 425 °C, we consider that the decomposition of the organic ligands leads to mass loss, and thus the selection of organic molecules is particularly important for designing hybrid luminescent materials with high thermal stability. In addition to the influence of the chemical stability, another channel leading to the decrease of the luminescence intensity with increasing temperature is thermally activated concentration quenching.[54,55] As shown in Fig. 5b, this unique 0D structure endows $(C_{24}H_{20}P)_2MnBr_4$ with a larger closest Mn···Mn distance of 10.447 Å, which allows all Mn^{2+} centers to emit spontaneously, and provides a platform for eliminating thermally activated concentration quenching by prohibiting energy migration with increasing temperature. Not only that, the activation energy ΔE of $(C_{24}H_{20}P)_2MnBr_4$ was calculated by using the following Arrhenius formula: $I_T/I_0 = [1 + A \times \exp(-\Delta E/kT)]^{-1}$, where I_0 and I_T are the emission intensity at RT and the experimental temperature, A is a constant, and k is the Boltzmann constant (k = 8.617 × 10^{-5} eV K^{-1}).[56]

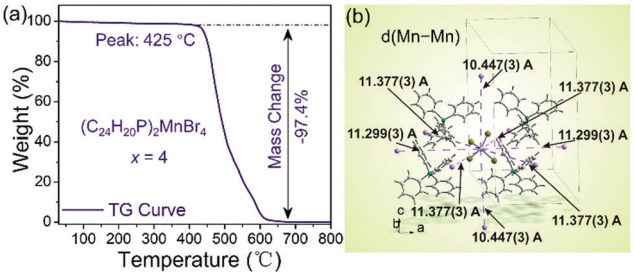

Fig. 5 (a) Thermogravimetric (TG) curve of $(C_{24}H_{20}P)_2MnBr_4$. (b) Crystal structures of $(C_{24}H_{20}P)_2MnBr_4$ with the closest Mn···Mn distance of 10.447 Å.

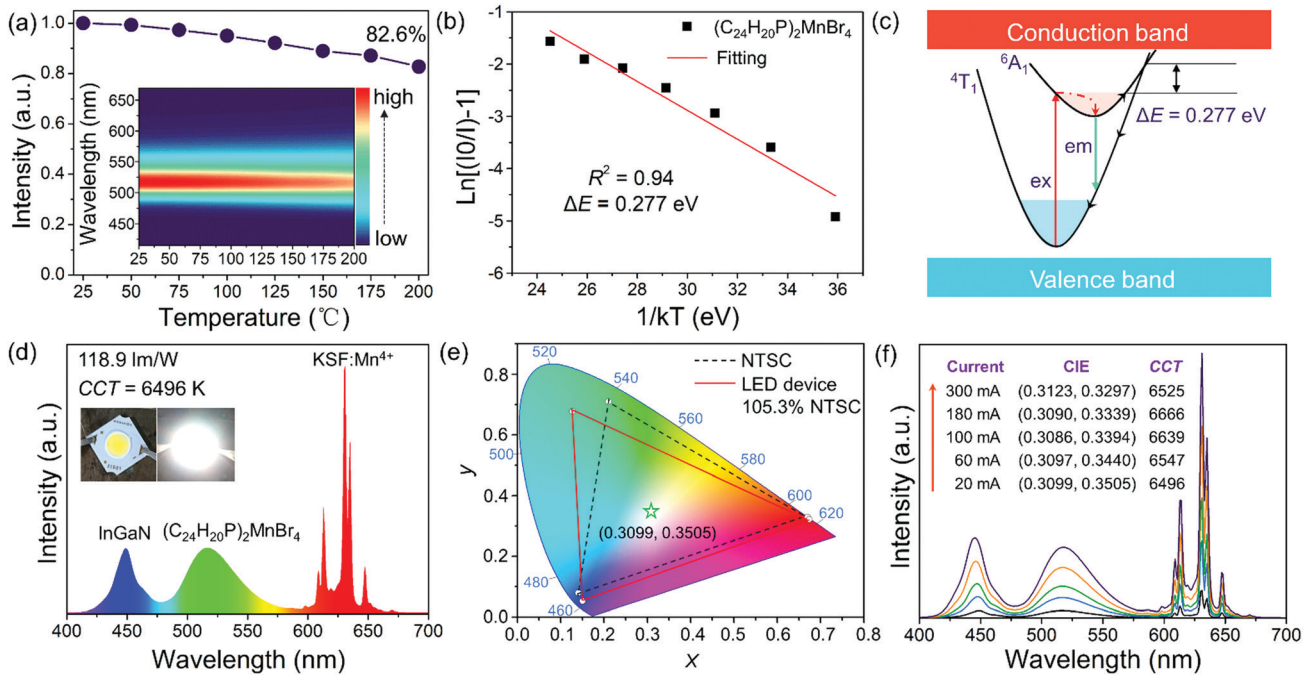

Fig. 4 (a) The temperature-dependent normalized PL intensity of $(C_{24}H_{20}P)_2MnBr_4$, and the inset showing a visual TQ behavior. (b) The thermal activation energy ΔE of $(C_{24}H_{20}P)_2MnBr_4$ analyzed by using the Arrhenius equation. (c) Configurational coordination diagram showing the thermal quenching of Mn^{2+} emission. (d) Emission spectrum and photographs of the fabricated white LED device based on $(C_{24}H_{20}P)_2MnBr_4$, K_2SiF_6:Mn^{4+} and an InGaN chip (λ_{em} = 450 nm). (e) The color gamut of the NTSC standard (black dotted line) and the fabricated white LED (red line, 104%) in the CIE 1931 system. (f) Emission spectra of the white LED under different driving currents from 20 to 300 mA.

The value of ΔE is obtained to be 0.277 eV (Fig. 4b), and the configurational coordinate diagram of Mn^{2+} can be used to understand the thermal quenching property. As shown in Fig. 4c, the electrons transition from $^4T_1$ to $^6A_1$ under light excitation, and then the excited electrons relax to the lowest energy level of $^6A_1$ through vibrational relaxation, and eventually back to the ground state of $^4T_1$, accompanied by the radiative transition of Mn^{2+}. Importantly, a nonradiative transition will occur when the excited electrons reach the crossing point of $^4T_1$ and $^6A_1$, resulting in the thermal quenching of Mn^{2+} emission. It is more difficult for the excited electrons to overcome the energy barrier when the value of ΔE is higher. Therefore, $(C_{24}H_{20}P)_2MnBr_4$ with a relatively large activation energy (ΔE = 0.277 eV) exhibits excellent thermal stability.

All the indicators indicate that $(C_{24}H_{20}P)_2MnBr_4$ can be employed as a desirable narrow-band green emitter for LED displays. As we all know, the water stability and blue light stability of $(C_{24}H_{20}P)_2MnBr_4$ are very important for LED applications. Here, the emission intensity maintains 67.9% of the pristine value over an aging time of 120 h at 85% relative humidity, as shown in Fig. S8 (ESI†). Meanwhile, we encapsulated a single-component LED device using $(C_{24}H_{20}P)_2MnBr_4$ and a blue chip to evaluate the blue light stability (Fig. S9, ESI†). After the LED device is continuously operated for 12 hours under a current of 20 mA, the luminous intensity still maintains 49.8% of the initial intensity, indicating that $(C_{24}H_{20}P)_2MnBr_4$ has relatively good blue light stability. In addition, the white LED device fabricated from $(C_{24}H_{20}P)_2MnBr_4$, K_2SiF_6:Mn^{4+} and an InGaN chip (λ_{em} = 450 nm) presents a high luminous efficiency of 118.9 lm W^{-1} and a suitable correlated color temperature (CCT) of 6496 K, and the corresponding photographs are shown in the inset of Fig. 4d. Importantly, the white LED device covers a wide color gamut of 105.3% NTSC in the CIE 1931 color space, as shown in Fig. 4e, which indicates that $(C_{24}H_{20}P)_2MnBr_4$ has great potential for practical applications as LCD backlights. In order to further evaluate its performance in high-power white LED applications, the emission spectra were measured under different currents. The current-dependent emission spectra from 20 to 300 mA change synchronously (Fig. 4f), and their CCT and CIE chromaticity coordinates have not changed significantly. It can be concluded that the narrow-band green emitting $(C_{24}H_{20}P)_2MnBr_4$ is a promising candidate for high-performance LEDs.

4. Conclusions

In summary, 0D Mn^{2+}-based metal halides $(C_{24}H_{20}P)_2MnCl_{4-x}Br_x$ (x = 0, 1, 2, 3, 4) with bright and stable narrow-band green emission at 518 nm have been reported, emphasizing the effect of Cl/Br modification on the PLQYs and lifetimes and unveiling the origin of thermal quenching behaviors. The nature of the halogen has been confirmed as a core factor to tune the PL behaviors, and the optimum Mn^{2+} emission with a high PLQY of 99.8% and a short lifetime of 0.372 ms can be achieved in $(C_{24}H_{20}P)_2MnBr_4$. According to the theoretical results, the calculated bandgap of $(C_{24}H_{20}P)_2MnBr_4$ is 3.57 eV, which is close to the optical band gap obtained experimentally. Remarkably, it is concluded that the synergistic effect of good chemical stability of organic groups, a long Mn···Mn distance of 10.447 Å and a relatively large activation energy (ΔE = 0.277 eV) provides a platform for achieving excellent thermal stability in $(C_{24}H_{20}P)_2MnBr_4$. Based on that, an as-fabricated white LED device with a high luminous efficacy of 118.9 lm W^{-1} and a wide color gamut of 105.3% NTSC can be obtained, suggesting that $(C_{24}H_{20}P)_2MnBr_4$ can be employed as a desirable narrow-band green emitter for LED displays. This work provides a versatile insight into tailoring halogens to control the PL properties, and exposes a deep understanding of thermal quenching behaviors for 0D Mn^{2+}-based metal halides.

Conflicts of interest

There are no conflicts to declare.

Acknowledgements

The present work was financially supported by the Natural Science Foundation of China (21871167), and 1331 Project of Shanxi Province and the Postgraduate Innovation Project of Shanxi Normal University (2019XBY018), and funded by RFBR according to the research project no. 19-52-80003.

Notes and references

1 S. Yakunin, L. Protesescu, F. Krieg, M. I. Bodnarchuk, G. Nedelcu, M. Humer, G. De Luca, M. Fiebig, W. Heiss and M. V. Kovalenko, *Nat. Commun.*, 2015, **6**, 8056.
2 M. V. Kovalenko, L. Protesescu and M. I. Bodnarchuk, *Science*, 2017, **358**, 745–750.
3 Q. Zhang and Y. Yin, *ACS Cent. Sci.*, 2018, **4**, 668–679.
4 Q. Fan, G. V. Biesold-McGee, J. Ma, Q. Xu, S. Pan, J. Peng and Z. Lin, *Angew. Chem., Int. Ed.*, 2020, **59**, 1030–1046.
5 S. Ghosh and B. Pradhan, *ChemNanoMat*, 2019, **5**, 300–312.
6 J. J. Luo, X. M. Wang, S. R. Li, J. Liu, Y. M. Guo, G. D. Niu, L. Yao, Y. H. Fu, L. Gao, Q. S. Dong, C. Y. Zhao, M. Y. Leng, F. S. Ma, W. X. Liang, L. D. Wang, S. Y. Jin, J. B. Han, L. J. Zhang, J. Etheridge, J. B. Wang, Y. F. Yan, E. H. Sargent and J. Tang, *Nature*, 2018, **563**, 541–545.
7 L. N. Quan, B. P. Rand, R. H. Friend, S. G. Mhaisalkar, T. W. Lee and E. H. Sargent, *Chem. Rev.*, 2019, **119**, 7444–7477.
8 V. Morad, S. Yakunin and M. V. Kovalenko, *ACS Mater. Lett.*, 2020, **2**, 845–852.
9 H. Yin, Y. M. Xian, Y. L. Zhang, W. Z. Li and J. D. Fan, *Sol. RRL*, 2019, **3**, 1900148.
10 C. K. Zhou, H. Lin, S. Lee, M. Chaaban and B. W. Ma, *Mater. Res. Lett.*, 2018, **6**, 552–569.
11 H. R. Lin, C. K. Zhou, Y. Tian, T. Siegrist and B. W. Ma, *ACS Energy Lett.*, 2017, **3**, 54–62.
12 M. I. Saidaminov, O. F. Mohammed and O. M. Bakr, *ACS Energy Lett.*, 2017, **2**, 889–896.

13 M. Lyu, J. H. Yun, P. Chen, M. Hao and L. Wang, *Adv. Energy Mater.*, 2017, **7**, 1602512.
14 G. J. Zhou, B. B. Su, J. L. Huang, Q. Y. Zhang and Z. G. Xia, *Mater. Sci. Eng., R*, 2020, **141**, 100548.
15 M. D. Smith, B. A. Connor and H. I. Karunadasa, *Chem. Rev.*, 2019, **119**, 3104–3139.
16 Y. Zhou, J. Chen, O. M. Bakr and H. T. Sun, *Chem. Mater.*, 2018, **30**, 6589–6613.
17 G. J. Zhou, X. X. Jiang, M. Molokeev, Z. S. Lin, J. Zhao, J. Wang and Z. G. Xia, *Chem. Mater.*, 2019, **31**, 5788–5795.
18 Z. Y. Li, Y. Li, P. Liang, T. L. Zhou, L. Wang and R.-J. Xie, *Chem. Mater.*, 2019, **31**, 9363–9371.
19 C. K. Zhou, M. Worku, J. Neu, H. R. Lin, Y. Tian, S. Lee, Y. Zhou, D. Han, S. Y. Chen, A. Hao, P. I. Djurovich, T. Siegrist, M. H. Du and B. W. Ma, *Chem. Mater.*, 2018, **30**, 2374–2378.
20 R. L. Zhang, X. Mao, D. Y. Zheng, Y. Yang, S. Q. Yang and K. L. Han, *Laser Photonics Rev.*, 2020, **14**, 2000027.
21 Z. S. Luo, Q. Li, L. M. Zhang, X. T. Wu, L. Tan, C. Zou, Y. J. Liu and Z. W. Quan, *Small*, 2020, **16**, 1905226.
22 L. Lian, M. Zheng, P. Zhang, Z. Zheng, K. Du, W. Lei, J. Gao, G. Niu, D. Zhang, T. Zhai, S. Jin, J. Tang, X. Zhang and J. Zhang, *Chem. Mater.*, 2020, **32**, 3462–3468.
23 A. Noculak, V. Morad, K. M. McCall, S. Yakunin, Y. Shynkarenko, M. Worle and M. V. Kovalenko, *Chem. Mater.*, 2020, **32**, 5118–5124.
24 L. Zhou, J. F. Liao, Z. G. Huang, J. H. Wei, X. D. Wang, W. G. Li, H. Y. Chen, D. B. Kuang and C. Y. Su, *Angew. Chem., Int. Ed.*, 2019, **58**, 5277–5281.
25 M. D. Smith and H. I. Karunadasa, *Acc. Chem. Res.*, 2018, **51**, 619–627.
26 L. J. Xu, C. Z. Sun, H. Xiao, Y. Wu and Z. N. Chen, *Adv. Mater.*, 2017, **29**, 1605739.
27 V. Morad, I. Cherniukh, L. Pöttschacher, Y. Shynkarenko, S. Yakunin and M. V. Kovalenko, *Chem. Mater.*, 2019, **31**, 10161–10169.
28 L. L. Mao, P. J. Guo, S. X. Wang, A. K. Cheetham and R. Seshadri, *J. Am. Chem. Soc.*, 2020, **142**, 13582–13589.
29 G. J. Zhou, Z. Y. Liu, J. L. Huang, M. S. Molokeev, Z. W. Xiao, C. G. Ma and Z. G. Xia, *J. Phys. Chem. Lett.*, 2020, **11**, 5956–5962.
30 B. B. Su, M. S. Molokeev and Z. G. Xia, *J. Mater. Chem. C*, 2019, **7**, 11220–11226.
31 Y. Zhang, W. Q. Liao, D. W. Fu, H. Y. Ye, Z. N. Chen and R. G. Xiong, *J. Am. Chem. Soc.*, 2015, **137**, 4928–4931.
32 M. Z. Li, J. Zhou, M. S. Molokeev, X. X. Jiang, Z. S. Lin, J. Zhao and Z. G. Xia, *Inorg. Chem.*, 2019, **58**, 13464–13470.
33 L. Xu, J. X. Gao, X. G. Chen, X. N. Hua and W. Q. Liao, *Dalton Trans.*, 2018, **47**, 16995–17003.
34 A. Jana, S. Zhumagali, Q. K. Ba, A. S. Nissimagoudar and K. S. Kim, *J. Mater. Chem. A*, 2019, **7**, 26504–26512.
35 B. B. Su, G. J. Zhou, J. L. Huang, E. H. Song, A. Nag and Z. G. Xia, *Laser Photonics Rev.*, 2020, 2000334.
36 G. Kresse and J. Furthmuller, *Phys. Rev. B: Condens. Matter Mater. Phys.*, 1996, **54**, 11169–11186.
37 G. Kresse and J. Hafner, *Phys. Rev. B: Condens. Matter Mater. Phys.*, 1993, **48**, 13115–13118.
38 G. Kresse and J. Furthmiiller, *Comput. Mater. Sci.*, 1996, **6**, 15–50.
39 G. Kresse and D. Joubert, *Phys. Rev. B: Condens. Matter Mater. Phys.*, 1999, **59**, 1758–1775.
40 P. E. Blochl, *Phys. Rev. B: Condens. Matter Mater. Phys.*, 1994, **50**, 17953–17979.
41 J. P. Perdew, K. Burke and M. Ernzerhof, *Phys. Rev. Lett.*, 1996, **77**, 3865–3868.
42 S. Grimme, J. Antony, S. Ehrlich and H. Krieg, *J. Chem. Phys.*, 2010, **132**, 154104.
43 S. Grimme, *Wiley Interdiscip. Rev.: Comput. Mol. Sci.*, 2011, **1**, 211–228.
44 J. Heyd, G. E. Scuseria and M. Ernzerhof, *J. Chem. Phys.*, 2003, **118**, 8207–8215.
45 L. K. Gong, Q. Q. Hu, F. Q. Huang, Z. Z. Zhang, N. N. Shen, B. Hu, Y. Song, Z. P. Wang, K. Z. Du and X. Y. Huang, *Chem. Commun.*, 2019, **55**, 7303–7306.
46 S. X. Li, L. Wang, D. M. Tang, Y. J. Cho, X. J. Liu, X. T. Zhou, L. Lu, L. Zhang, T. Takeda, N. Hirosaki and R. J. Xie, *Chem. Mater.*, 2018, **30**, 494–505.
47 M. Zhao, Q. Y. Zhang and Z. G. Xia, *Mater. Today*, 2020, **40**, 246–265.
48 G. J. Zhou, X. F. Jia, S. Q. Guo, M. S. Molokeev, J. Y. Zhang and Z. G. Xia, *J. Phys. Chem. Lett.*, 2019, **10**, 4706–4712.
49 Y. Y. Zhou, E. H. Song, M. Brik, Y. Y. Wang, T. Hu, Z. G. Xia and Q. Y. Zhang, *J. Mater. Chem. C*, 2019, **7**, 9203–9210.
50 D. Han, H. L. Shi, W. M. Ming, C. K. Zhou, B. W. Ma, B. Saparov, Y. Z. Ma, S. Y. Chen and M. H. Du, *J. Mater. Chem. C*, 2018, **6**, 6398–6405.
51 M. Z. Li, J. Zhou, G. J. Zhou, M. S. Molokeev, J. Zhao, V. Morad, M. V. Kovalenko and Z. G. Xia, *Angew. Chem., Int. Ed.*, 2019, **58**, 18670–18675.
52 Y. Wei, Z. Y. Cheng and J. Lin, *Chem. Soc. Rev.*, 2019, **48**, 310–350.
53 J. R. Hao, X. Y. Qu, L. Qiu, G. G. Li, Y. Wei, G. C. Xing, H. Q. Wang, C. J. Yan, H. S. Jang, Z. Y. Cheng and J. Lin, *Adv. Opt. Mater.*, 2018, **7**, 1801323.
54 V. Bachmann, C. Ronda and A. Meijerink, *Chem. Mater.*, 2009, **21**, 2077–2084.
55 J. W. Qiao, J. Zhao, Q. L. Liu and Z. G. Xia, *J. Rare Earths*, 2019, **37**, 565–572.
56 S. Bhushan and M. V. Chukichev, *J. Mater. Sci. Lett.*, 1988, **7**, 319–321.